

Electron beams traversing spherical nanoparticles: analytic and numerical treatment

P. Elli Stamatopoulou ^{1,*} Wenhua Zhao* ^{2,3} Álvaro Rodríguez Echarri ³
N. Asger Mortensen ^{1,4} Kurt Busch ^{5,3,†} Christos Tserkezis ¹ and Christian Wolff ^{1,‡}

¹*POLIMA—Center for Polariton-driven Light-Matter Interactions,
University of Southern Denmark, Campusvej 55, DK-5230 Odense M, Denmark*

²*Humboldt-Universität zu Berlin, Institut für Physik,
AG Theoretische Optik und Photonik, 12489 Berlin, Germany*

³*Max-Born-Institut, 12489 Berlin, Germany*

⁴*Danish Institute for Advanced Study, University of Southern Denmark, Campusvej 55, DK-5230 Odense M, Denmark*

⁵*Humboldt-Universität zu Berlin, Institut für Physik,
AG Theoretische Optik und Photonik, 12489 Berlin, Germany*

(Dated: September 12, 2023)

We present an analytic, Mie-theory based solution for the energy-loss and the photon-emission probabilities in the interaction of spherical nanoparticles with electrons passing nearby and through them, in both cathodoluminescence (CL) and electron energy-loss spectroscopies (EELS). In particular, we focus on the case of penetrating electron trajectories, for which the complete fully electrodynamic and relativistic formalism has not been reported as yet. We exhibit the efficiency of this method in describing collective excitations in matter through calculations for a dispersive and lossy system, namely a sphere described by a Drude permittivity, and discuss possible complications when computing contributions from higher-order modes. Subsequently, we use the analytic solution to corroborate the implementation of electron-beam sources in a state-of-the-art numerical method for problems in electrodynamics, the discontinuous Galerkin time-domain (DGTD) method. We show that the two approaches produce spectra in good mutual agreement, and demonstrate the versatility of DGTD via simulations of spherical nanoparticles characterized by surface roughness. The possibility of simultaneously employing both kinds of calculations (analytic and numerical) facilitates a better understanding of the rich optical response of nanophotonic architectures excited by fast electron beams.

I. INTRODUCTION

In recent decades, electron-beam spectroscopy has emerged as a revolutionary tool for the optical characterization of materials. Swift electrons passing in close proximity or through a specimen, undergo energy loss owing to energy transfer to the optical modes sustained in the material [1]. From localized and propagating surface plasmons in metallic structures [2–5], to Mie resonances in dielectric resonators [6–8] and phonon polaritons in polar crystals [9–11], electron-beam spectroscopy has proven quintessential for mapping collective excitations in a broad spectral range that spans from ultraviolet to far-infrared frequencies.

With the diffraction limit ultimately being controlled by the de Broglie wavelength, highly energetic electrons are excellent probes to study the optical properties of truly nanoscale structures, with atomic spatial resolution and sub-meV energy resolution [12, 13]. In electron energy-loss spectroscopy (EELS), the sample is excited by a high-energy (30 – 300 keV) electron beam and the energy lost to the interaction is measured in a transmission electron microscope (TEM) setup [14, 15]. EELS allows, thereby, the detection of both radiative and dark modes, including longitudinal bulk plasmons (BPs) [16], breathing modes [17], or antibonding modes in nanoparticle (NP) dimers [18]. Optical excitations in thick samples can be imaged in cathodoluminescence (CL) spectroscopy, performed in scanning electron microscopes

(SEMs) at intermediate beam energies (1–50 keV) [1, 12]. In CL measurements, the signal collected is the result of far-field photon emission from the sample, originating from the radiative decay of the excited modes. Recent advances in instrumentation have even added temporal resolution in EEL and CL spectra, introducing the field of ultrafast electron microscopy (UEM) [19, 20].

Considering the recent progress in electron spectroscopy techniques, robust analytic and computational tools are evidently required to interpret the plethora of experimental data. While first theoretical efforts were performed within the non-retarded approximation for the description of plasmons in thin films [3], the theory was gradually generalized to account for collective excitations in diverse media and geometries [21, 22], also considering retardation effects [23, 24]. Quantum approaches [25, 26] and analytic solutions including relativistic effects for simple geometries were later developed [27, 28], allowing the combination of high-velocity electron beams with both common and less conventional materials, including dielectric media, polar crystals, graphene and other two-dimensional (2D) materials [8, 11, 29, 30]. Most theoretical relativistic descriptions have focused on aloof electron trajectories, that do not penetrate the specimen, in contrast to experimental practices, where the electron beam is typically scanned over the entire sample area [14]. However, aloof electron trajectories oftentimes fail to capture intriguing phenomena associated with bulk properties, such as BPs and bulk phonons [9, 18], and other sources of electron-induced photon emission, like

Cherenkov or transition radiation [27, 31–33].

Despite the undeniable advantage of analytic solutions in data analysis, their applicability is limited to a handful of highly symmetric geometries. Over the years, different numerical schemes have been consolidated to complement analytic approaches in simulating the electromagnetic properties of nanophotonic systems of diverse shapes and forms [34], such as the boundary element method (BEM) [35, 36], the finite element method (FEM) [37, 38], or the finite-difference frequency-domain (FDFD) and finite-difference time-domain (FDTD) methods [39, 40]. An alternative route is offered by the discontinuous Galerkin time-domain (DGTD) method, which employs the Galerkin scheme to solve Maxwell’s equations in the time domain [41–45]. This method combines the flexible space discretization of finite elements, with the memory efficiency and the ability to include nonlinearities, characteristic of time-domain methods. As a consequence, DGTD offers great versatility in simulating objects of complex geometry and nonlinear response.

In this work, we present and compare an analytic approach and the DGTD method for the study of spherical nanostructures excited by a loof and penetrating electron beams. Following the work of García de Abajo for loof electron beams [28], we derive analytic formulas for the energy loss and photon emission probability, generalized here to account for penetrating trajectories. We then validate the implementation of electron-beam excitation of nanostructures in DGTD [42] by comparing the EEL and CL spectra produced by the two methods for a perfectly spherical plasmonic NP featuring localized surface plasmons (LSPs) and BPs. Finally, we apply the numerical method to study the optical response of a NP with surface roughness, showcasing the ability of the DGTD method to emulate scenarios aligned with realistic experimental conditions that involve imperfect structures [46, 47].

II. METHODS

A. Analytic approach

As a first step to examine the agreement and complementarity of analytic and numerical tools, we outline the modeling of the physical system and the assumptions made in each method. As a testbed, we consider a perfectly spherical metal NP of radius R suspended in air. The NP is characterized by a unity relative permeability ($\mu = 1$), while its relative permittivity depends on the angular frequency ω as described by the Drude model

$$\varepsilon(\omega) = 1 - \frac{\omega_p^2}{\omega(\omega + i\tau^{-1})}, \quad (1)$$

with plasma frequency ω_p and damping rate τ^{-1} .

In the analytic calculation, the electron beam is modeled as a single point particle that carries the elementary

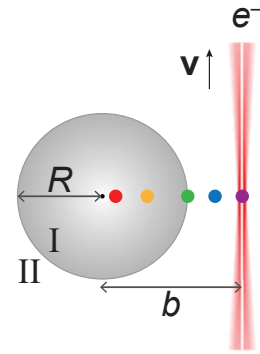


FIG. 1. Schematic illustration of the geometry under study; a metallic NP of radius $R = 75$ nm, and permittivity described by the Drude model of Eq. (1), is excited by an electron beam passing with velocity \mathbf{v} at impact parameter b with respect to its center. The color dots correspond to the selection of impact parameters examined in our study. Labels I and II indicate the region inside the NP and the surrounding medium (air), respectively.

charge $-e$. We assume that it travels with constant velocity \mathbf{v} , say along the z -axis, following thus a trajectory $\mathbf{r}_e = \mathbf{r}_0 + \mathbf{v}t$, where $\mathbf{r}_0 = (b, \phi_0, z = -\infty)$ is its initial position in cylindrical coordinates. The impact parameter b indicates the distance between the electron trajectory and the center of the sphere, as shown in the schematics of Fig. 1. In passing, we mention that the angular coordinate ϕ_0 need not be specified, as it does not enter the calculation, due to the symmetry of the problem.

The fast electron drives plasmon oscillations in the metal, generating an induced electric and magnetic field, \mathbf{E}_{ind} and \mathbf{H}_{ind} respectively, eventually resulting in the emission of radiation to the environment (labeled as region II in Fig. 1). Following the basic steps of Mie theory [48], one can decompose the induced electromagnetic field into transverse electric (TE) and transverse magnetic (TM) components. In region II the induced fields take the general form of outgoing spherical waves [49]

$$\mathbf{E}_{\text{ind}}^{\text{II}}(\mathbf{r}) = \sum_{\ell=1}^{\infty} \sum_{m=-\ell}^{+\ell} \left\{ b_{\ell m}^{\text{II}} h_{\ell}^{+}(k_0 r) \mathbf{X}_{\ell m}(\hat{\mathbf{r}}) + \frac{i}{k_0} a_{\ell m}^{\text{II}} \nabla \times h_{\ell}^{+}(k_0 r) \mathbf{X}_{\ell m}(\hat{\mathbf{r}}) \right\} \quad (2a)$$

$$\mathbf{H}_{\text{ind}}^{\text{II}}(\mathbf{r}) = \frac{1}{Z_0} \sum_{\ell=1}^{\infty} \sum_{m=-\ell}^{+\ell} \left\{ a_{\ell m}^{\text{II}} h_{\ell}^{+}(k_0 r) \mathbf{X}_{\ell m}(\hat{\mathbf{r}}) - \frac{i}{k_0} b_{\ell m}^{\text{II}} \nabla \times h_{\ell}^{+}(k_0 r) \mathbf{X}_{\ell m}(\hat{\mathbf{r}}) \right\}, \quad (2b)$$

where ℓ, m are the angular momentum quantum numbers, and $a/b_{\ell m}^{\text{II}}$ denote the expansion coefficients of the TE/TM components corresponding to modes of electric/magnetic multipole character (see the appendix for the analytic expressions). Furthermore, in Eqs. (2) h_{ℓ}^{+} is the spherical Hankel function of the first kind, $\mathbf{X}_{\ell m}$ are the vector spherical harmonics, $k_0 = \omega/c$, is the wave

number in free space, $c = 1/\sqrt{\varepsilon_0\mu_0}$ the speed of light in vacuum, where ε_0 and μ_0 denote the vacuum permittivity and permeability, respectively, and $Z_0 = \sqrt{\mu_0/\varepsilon_0}$ is the impedance in free space. Details about the field expansions can be found in section S.I of the Supporting Information (SI).

The energy radiated in the far field can be found by integrating the Poynting flux at a spherical surface of radius $r \rightarrow \infty$, in the normal direction $\hat{\mathbf{r}}$. Then the (CL) probability of collecting a photon of energy $\hbar\omega$ is given by

$$\Gamma_{\text{CL}}(\omega) = \frac{r^2}{\pi\hbar\omega} \int d\Omega \text{Re}\{\mathbf{E}_{\text{ind}}^{\text{II}}(\mathbf{r}, \omega) \times \mathbf{H}_{\text{ind}}^{\text{II}*}(\mathbf{r}, \omega)\} \cdot \hat{\mathbf{r}}, \quad (3)$$

where $d\Omega$ denotes the infinitesimal solid angle. By inserting Eqs. (2) into Eq. (3), and evaluating the result in the far field ($k_0 r \rightarrow \infty$), we find

$$\Gamma_{\text{CL}}(\omega) = \frac{1}{\pi\hbar\omega Z_0 k_0^2} \sum_{\ell=1}^{\infty} \sum_{m=-\ell}^{+\ell} \left\{ |b_{\ell m}^{\text{II}}|^2 + |a_{\ell m}^{\text{II}}|^2 \right\}. \quad (4)$$

$$\Gamma_{\text{bulk}}(\omega) = \frac{e^2 z_e}{2\pi^2 \varepsilon_0 \hbar v^2} \text{Im} \left\{ \frac{1}{\gamma_0^2} \ln \left(\left[\frac{q_c \gamma_0 v}{\omega} \right]^2 + 1 \right) - \frac{1}{\gamma^2 \varepsilon} \ln \left(\left[\frac{q_c \gamma v}{\omega} \right]^2 + 1 \right) \right\}, \quad (7a)$$

$$\Gamma_{\text{surf}}(\omega) = \frac{e}{\pi\hbar\omega} \text{Re} \sum_{\ell=1}^{\infty} \sum_{m=-\ell}^{+\ell} \left\{ \frac{K_m(\omega b/[v\gamma_0])}{ik_0 \sqrt{\ell(\ell+1)}} \left[mb_{\ell m}^{\text{II}} \mathcal{M}_{\ell m}^* - a_{\ell m}^{\text{II}} \frac{\mathcal{N}_{\ell m}^*}{\beta\gamma_0} \right] - \int_{-z_e}^{z_e} dz \frac{\exp(-i\omega z/v)}{\sqrt{\ell(\ell+1)}} \left[mb_{\ell m}^{\text{II}} h_{\ell}^+(k_0 r) Y_{\ell}^m(\theta, 0) - \frac{a_{\ell m}^{\text{II}}}{k_0 b} \{ \mathcal{H}_{\ell m}^+(k_0 z) + \mathcal{H}_{\ell m}^-(k_0 z) \} \right] \right\}, \quad (7b)$$

and

$$\Gamma_{\text{Begr}}(\omega) = \frac{e}{\pi\hbar\omega} \text{Re} \sum_{\ell=1}^{\infty} \sum_{m=-\ell}^{+\ell} \int_{-z_e}^{z_e} dz \frac{\exp(-i\omega z/v)}{\sqrt{\ell(\ell+1)}} \left[mb_{\ell m}^{\text{I}} j_{\ell}(kr) Y_{\ell}^m(\theta, 0) - \frac{a_{\ell m}^{\text{I}}}{kb} \{ \mathcal{J}_{\ell m}^+(kz) + \mathcal{J}_{\ell m}^-(kz) \} \right]. \quad (7c)$$

Here, $2z_e = 2\sqrt{R^2 - b^2}$ is the length of the electron path inside the NP, and $\gamma = 1/[1 - \varepsilon\beta^2]^{1/2}$ with $\beta = v/c$ are the Lorentz kinematic factors (γ_0 is evaluated in free space). In Eqs. (7b) and (7c) K_m is the modified Bessel function of the second kind and Y_{ℓ}^m are the spherical harmonics. In addition, we have set $r = \sqrt{b^2 + z^2}$, and $\theta = \arccos(z/r)$, while analytic expressions for coefficients $a/b_{\ell m}^{\text{I}}$, $\mathcal{M}_{\ell m}$, $\mathcal{N}_{\ell m}$, $\mathcal{H}_{\ell m}^{\pm}$, and $\mathcal{J}_{\ell m}^{\pm}$ can be found in the appendix.

It is important to note here that the aforementioned decomposition of the EEL spectra introduces a free parameter; assuming that upon losing energy $\hbar\omega$ the electron transfers a transverse (with respect to the electron

Apart from the emission of radiation, part of the energy transferred to the optical modes of the NP dissipates non-radiatively, owing to the intrinsic losses within the material. The total energy lost can be calculated by the work done by the electron against the induced field along the entire electron trajectory. Then the (EEL) probability of the electron losing energy $\hbar\omega$ is given by

$$\Gamma_{\text{EELS}}(\omega) = \frac{e}{\pi\hbar\omega} \int dt \text{Re}\{ \exp(-i\omega t) \mathbf{v} \cdot \mathbf{E}_{\text{ind}}(\mathbf{r}_e, \omega) \}. \quad (5)$$

The integral in Eq. (5) can be decomposed into three terms (see details in section S.I of the SI)

$$\Gamma_{\text{EELS}}(\omega) = \Gamma_{\text{bulk}}(\omega) + \Gamma_{\text{surf}}(\omega) + \Gamma_{\text{Begr}}(\omega). \quad (6)$$

Here, Γ_{bulk} is related to the bulk modes of the unbound medium, reduced by the Begrenzung term Γ_{Begr} that accounts for the presence of a boundary [50]. The Γ_{surf} term contains the contribution from modes excited by the part of the electron trajectory lying externally to the NP, and is, thus, associated with the excitation of LSPs. The terms entering Eq. (6) are given by the following formulas

trajectory) momentum q to excite an optical mode, q_c is the maximum transverse momentum collected. In an experiment, the momentum cutoff is determined by the half-aperture collection angle φ of the microscope spectrometer, as

$$\hbar q_c \approx \sqrt{(m_e v \varphi)^2 + (\hbar\omega/v)^2}, \quad (8)$$

where m_e is the electron mass. We may freely choose the value for this momentum cutoff, making sure that it aligns with the typical values for the collection angle in scanning TEM (STEM) setups, which are in the order of a few mrad. Naturally, this introduces a level of arbitrariness in the EEL spectra, as various values of q_c lead to different peak intensities at the BP energy.

B. DGTD simulation

We complement our analytical work with numerical simulations of the electromagnetic problem of a NP excited by a moving Gaussian charge distribution. To this end, we employ the DGTD method (see details in section S.II of the SI), which combines a piecewise polynomial spatial interpolation on an unstructured tetrahedral mesh with a Runge–Kutta time integrator to obtain a high-order accurate explicit solver for Maxwell’s equations in time domain

$$\partial_t \mathbf{H}(\mathbf{r}, t) = -\mu_0^{-1} \mu^{-1}(\mathbf{r}) \nabla \times \mathbf{E}(\mathbf{r}, t), \quad (9a)$$

$$\partial_t \mathbf{E}(\mathbf{r}, t) = \varepsilon_0^{-1} \varepsilon^{-1}(\mathbf{r}) [\nabla \times \mathbf{H}(\mathbf{r}, t) - \mathbf{j}(\mathbf{r}, t)]. \quad (9b)$$

Here, \mathbf{j} is the total current density that encompasses both any current associated with the excitation source, as well as dispersive polarization currents. The resulting method is memory-efficient compared to traditional finite elements and especially well-suited for the calculation of wide-band spectra.

One key difference between the Mie-based theory and the DGTD simulations, which can potentially lead to deviations between the two approaches, is the implementation of the excitation source. In the numerical treatment, we model the electron beam with a Gaussian charge distribution of the form

$$\rho(\mathbf{r}) = -\frac{e}{\sigma_e^3 \sqrt{\pi^3}} \exp(-r^2/\sigma_e^2), \quad (10)$$

with width $\sigma_e = 5$ nm. This choice essentially prevents numerical artifacts arising when implementing a point-charge particle moving inside the simulation domain, while also being compatible with the typical spot size in CL experiments [8]. Thereby, we introduce a new spatial scale, which needs to be taken into account when it is comparable to the parameters related to the discretization of the computational domain, such as the mesh element size, as well as the characteristic lengths of the physical system, e.g. the radius of the NP and the impact parameter. For very large distances between the electron and the NP (i.e., $b - R \gg \sigma_e$), the source resembles a point charge and we, therefore, expect an excellent agreement with analytic results. However, in the opposite scenario, the finite width of the electron beam becomes important, and the corresponding fields do not accurately match those of a point charge.

III. RESULTS AND DISCUSSION

A. EEL and CL spectroscopy of perfectly spherical NPs

In what follows, we analyze the response of a metallic NP excited by a fast electron beam, as predicted by both the analytic and the numerical approach. We consider a smooth sphere of radius $R = 75$ nm with plasma

energy $\hbar\omega_p = 5$ eV and damping rate τ^{-1} corresponding to an energy of $\hbar\tau^{-1} = 50$ meV. The parameters mimic typical plasmonic metals and are chosen for the purpose of illustration, while the particular values have no consequences for our general conclusions. Fig. 2 shows the scattering spectrum (panel a) under plane-wave illumination, and the CL and EELS probability (panels b and c, respectively) calculated for a low electron velocity $v = 0.33c$ (kinetic energy ≈ 30 keV) intersecting the NP at $b = 35$ nm from its center. As suggested by Eq. (4), the total photon emission probability can be decomposed into contributions of pairwise orthogonal electric and magnetic multipoles of order ℓ . Fig. 2b reveals that the CL spectrum is composed of the contributions of the first four ($\ell = 1, 2, 3, 4$) electric-type modes, appearing at approximately 2, 2.8, 3.1, and 3.2 eV, associated with the excitation of LSP resonances, while higher-order ($\ell > 4$) multipoles contribute negligibly to the spectrum. In comparison with the scattering cross section of the NP shown in Fig. 2a (calculated using Mie theory [51]), the CL spectrum provides very similar information. This is somewhat expected, since both calculations are based on the collection of far-field radiation. We observe, nonetheless, two notable distinct features in the CL spectrum of Fig. 2b. Firstly, the electron source excites more efficiently the $\ell = 2$ and 3 modes, whereas in the scattering spectrum of Fig. 2a the dipolar mode peak features the highest intensity. The relative peak intensities in the CL and EEL spectra depend strongly on the impact parameter, which determines the arrangement of the polarization charges in the material [52]. Secondly, we observe a small redshift of the dipolar ($\ell = 1$) mode in CL due to retardation, stemming from the fact that the speed of the electron is only a fraction of the speed of light.

In Fig. 2c we present the EEL spectrum, decomposed as described in Eq. (6). In the zoom-in area of the figure we observe the excitation of numerous higher-order multipoles, appearing as sharp peaks at energies up to 3.5 eV. With increasing multipole order, the wavelength of the corresponding mode reduces, so higher-order modes experience the curved surface of the NP as increasingly more flat. As a result, they accumulate at the energy corresponding to that of a surface plasmon polariton (SPP) at a planar interface, at $\hbar\omega_{\text{spp}} = \hbar\omega_p/\sqrt{2} \approx 3.5$ eV. Above the SPP energy, the spectrum exhibits a pronounced peak at the BP energy $\hbar\omega_{\text{bp}} = \hbar\omega_p = 5$ eV, pertaining to the excitation of BPs in the volume of the NP. Since BPs are longitudinal modes, they do not couple to far-field radiation and, therefore, they can be detected only in EELS. At the same energy, we observe the expected negative peak related to the Begrenzung term, reducing the BP peak in the total EEL probability [50].

Having a clear picture of the origin of all spectral features, in Figs. 3a and b we compare the CL and EEL probability, respectively, of the same metal NP, as calculated employing the analytic (Mie) and the DGTD method. We test the agreement between the two calculations probing various impact parameters, that range from

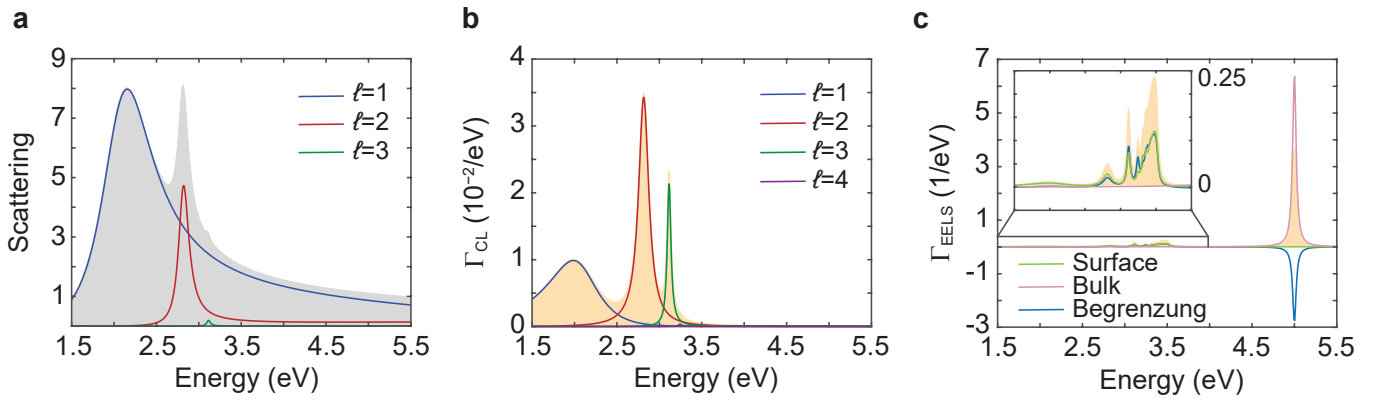


FIG. 2. (a) Scattering cross section, normalized to the geometrical cross section πR^2 , of the metallic NP of Fig. 1 under plane-wave excitation (gray shaded area). The spectrum is decomposed into the contributions from the first three multipoles (blue, red and green curves, for $\ell = 1, 2, 3$ respectively). (b) CL probability (yellow shaded area) decomposed into the contributions from the first four multipoles (blue, red, green, and violet curves). (c) EEL probability (yellow shaded area) decomposed into the surface, bulk, and Begrenzung contributions (blue, green and pink curves), with the inset focusing into the energy window 1 – 4 eV. The bulk term is given by Eq. (7a) for $q_c = 0.71 \text{ nm}^{-1}$. In (b) and (c) we consider an electron traveling with velocity $v = 0.33c$ (kinetic energy $\approx 30 \text{ keV}$) passing through the NP of Fig. 1 at impact parameter $b = 35 \text{ nm}$.

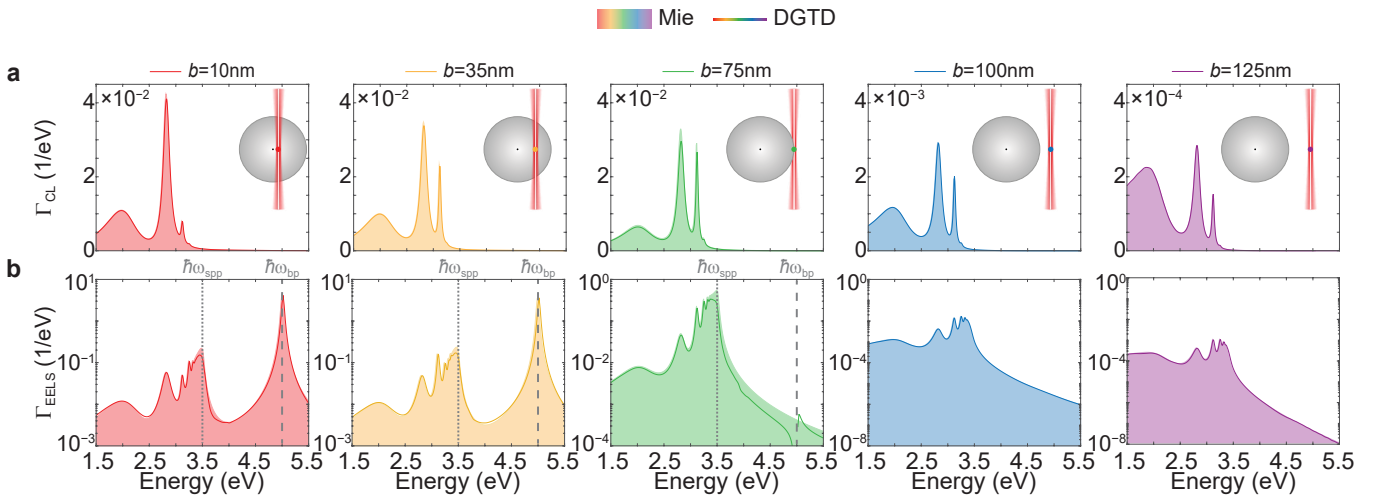


FIG. 3. (a) CL and (b) EEL probability in the interaction between the metallic NP of Fig. 1 and an electron traveling with velocity $v = 0.33c$ (kinetic energy $\approx 30 \text{ keV}$) considering 5 different impact parameters, as denoted in the labels and illustrated in the insets of each panel, and momentum cutoff $q_c = 0.71 \text{ nm}^{-1}$. The shaded areas correspond to results of the analytic Mie-type calculation, whereas the solid lines show the corresponding DGTD simulations. The vertical gray dotted and dashed lines in the three leftmost panels of (b) trace the energy of the SPP ($\hbar\omega_{\text{spp}} \approx 3.5 \text{ eV}$) and the BP mode ($\hbar\omega_{\text{bp}} = 5 \text{ eV}$), respectively.

$b = 125 \text{ nm}$ to 10 nm , corresponding to aloof electron trajectories (violet and blue spectra), grazing (green), and penetrating (yellow and red). Overall, the DGTD method reproduces the positions of the LSP modes and the corresponding CL probabilities of the Mie calculations. In Fig. 3a we show an excellent agreement in the CL spectra, with a relative error at around 1% for aloof and penetrating electron trajectories (see Table I). The highest error is acquired when the electron grazes the surface of the NP, passing exactly at $b = R$ (middle panel in Fig. 3a). This point reflects an important limit in the capabilities of the DGTD method; in the grazing trajectory, due to the finite width of the electron beam, half of

the Gaussian charge density distribution lies inside the NP, while the other half lies outside, leading to numerical inconsistencies. One may avoid this point, which is inevitably difficult to resolve, by slightly adjusting the impact parameter by half the Gaussian width.

Regarding compatibility of the EEL spectra, the two rightmost panels in Fig. 3b reveal an excellent agreement for aloof electron trajectories. We consistently find a higher error for grazing trajectories (middle panel in Fig. 3b); here, the EELS spectrum calculated with DGTD exhibits a numerical artifact at the BP energy (gray dashed line), resulting once again from the fact that only a fraction of the electron charge density dis-

TABLE I. Relative error [see Eq. (S.38) in the SI] between the analytic and the DGTD calculations of Γ_{CL} and Γ_{EELS} for varying b .

b (nm)	Γ_{CL} (%)	Γ_{EELS} (%)
10	1.26	9.75
35	1.06	6.17
75	8.23	28.87
100	1.06	1.02
125	1.07	1.93

tribution penetrates the NP, exciting only partially the bulk mode. A substantial deviation between the two methods is found in EEL spectra for both grazing and penetrating electron trajectories (three leftmost panels in Fig. 3b) between the SPP and the BP energy, denoted by the gray dotted and dashed lines, respectively. The disagreement is, naturally, reflected in the large relative errors presented in Table I accordingly. At these impact parameters, the condition $b - R \gg \sigma_e$ is not fulfilled, hence the field of the electron deviates considerably from that of a point charge. Moreover, the beam width σ_e becomes important compared to the mesh element size, since the surface of the NP is more finely discretized than the surrounding medium (see Fig. S4 in the SI). Finally, there exists an additional source of error in the evaluation of the BP contribution, that stems from the rather arbitrary choice of the transverse momentum cutoff q_c in the analytic approach. In contrast, in the DGTD implementation there is a respective internal limit, associated with σ_e . As a result, we consistently find higher relative errors in EELS in comparison with CL, and for grazing and penetrating electron trajectories as compared to aloof, probing both low-energy electron beams as in Fig 3, as well as higher energies that are more realistic for EEL measurements (see Fig. S.8 in the SI for CL and EEL spectra at energy 200 keV).

Admittedly, the accumulation point of high-order multipoles at $\hbar\omega_{\text{spp}}$ is hard to be resolved in both methods. On the one hand, the analytic Mie calculation assumes a moving point charge, which can, in principle, excite an infinite number of multipoles, resulting in a sharp high-intensity peak at energy $\hbar\omega_{\text{spp}}$. On the other hand, the finite mesh size and beam width implemented in DGTD imposes a limitation to the number of multipoles that can be resolved for a given discretization, since high order multipoles associated with field variation shorter than the mesh element size at the surface cannot be captured without the use of very high order polynomials. In EELS and CL experiments, there exists an analogous limitation, associated with the finite width of the electron beam employed, as well as the geometric imperfections of the NP. The versatility of DGTD allows us not only to adjust the electron beam width according to the experimental setup, but also to mimic NPs with surface roughness, as we discuss in section III B. In the

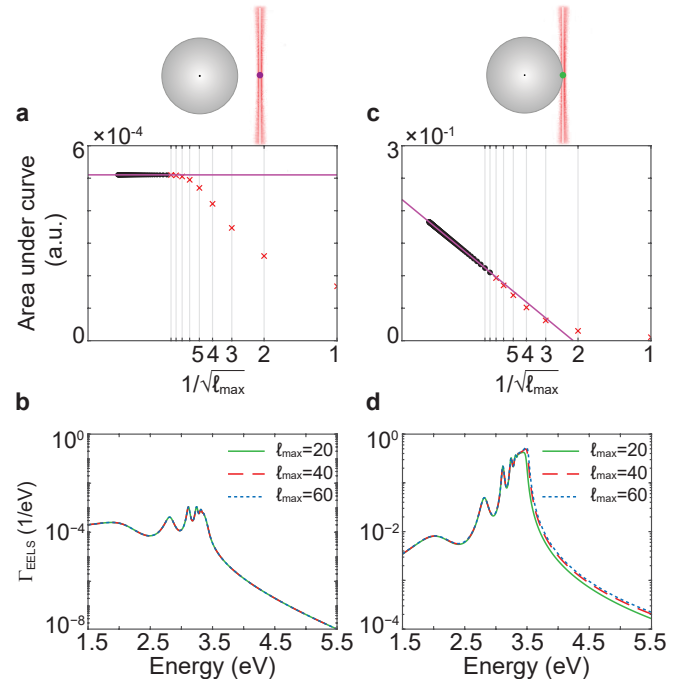


FIG. 4. (a, c) Area under the curve of the EEL spectra of Fig. 3b, (a) for the aloof electron trajectory at $b = 125$ nm, (c) for the grazing trajectory at $b = 75$ nm, showcasing the convergence of the EEL probability for increasing values of the multipole cutoff ℓ_{max} , plotted versus $1/\sqrt{\ell_{\text{max}}}$. In both panels, the magenta line is fitted to the data points marked as black bullets, while the red crosses represent data points excluded from the fitting. The vertical gray lines serve as guides to the eye for the position of $\ell_{\text{max}} = 1, 2 \dots 5$. (b, d) EEL probability calculated for impact parameters (b) $b = 125$ nm, and (d) $b = 75$ nm, and for selected values of ℓ_{max} , as denoted in the labels.

analytic approach, the smearing of higher-order modes and the overall quenching of the sharp peak at the accumulation point can too be reproduced, once we consider the nonlocal response of the material; this can be done particularly easily within Mie theory [53–55]. Nonlocal effects manifest as increased damping and uneven energy shifts of high-order modes, and, therefore, lead to the suppression of the individual modes, as well as the reduction of their overlap at $\hbar\omega_{\text{spp}}$ [56].

The difficulty in resolving the high-order multipoles even in the analytic calculation is clear in the convergence study presented in Figs. 4 and 5. Due to multipole orthogonality, increasing ℓ_{max} only ever adds signal. This suggests monitoring the total EEL spectrum integrated over energy (area under the curve) as a proxy for convergence. For aloof trajectories, the asymptotics of the Hankel functions suggest exponential convergence, which is in agreement with Figs. 4a and b; the EEL probability converges at $\ell_{\text{max}} = 10$. In contrast, Fig. 4c shows that in the case of the grazing trajectory the convergence order breaks down to a square root law. By extrapolation (magenta line) we can conclude that even for $\ell_{\text{max}} = 63$ the analytic result is still converged only up to

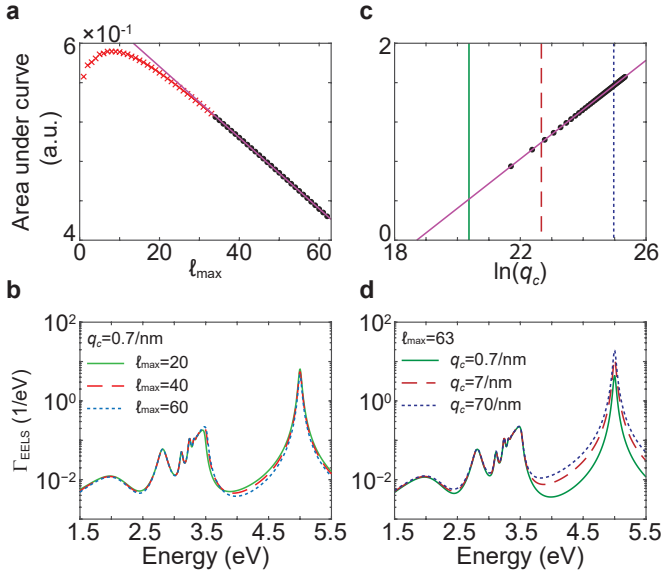


FIG. 5. (a, c) Area under the curve of the EEL spectrum of the leftmost panel in Fig. 3b ($b = 10 \text{ nm}$), showcasing the divergence of the EEL probability for increasing values of (a) the multipole cutoff ℓ_{\max} , and (c) the transverse momentum cutoff q_c plotted versus $\ln(q_c)$. The data follow a linear divergence trend with respect to their corresponding horizontal axes. In both panels, the magenta line is fitted to the data points marked as black bullets, while the red crosses represent data points excluded from the fitting. (b, d) EEL probability calculated at $b = 10 \text{ nm}$ for selected values of (b) ℓ_{\max} , and (d) q_c . In panels (a, b) we scan over ℓ_{\max} , while keeping a fixed value $q_c = 0.71 \text{ nm}^{-1}$, whereas in (c, d) we scan over q_c for a fixed value $\ell_{\max} = 63$, as denoted in the labels. In panel (c) the vertical lines correspond to the selected q_c values presented in (d), following the same color coding.

about 15%. Fig. 4d corroborates that the area missing from the converged value corresponds to the higher-order modes piling up at the SPP energy. Finally, we note that Fig. 4a exhibits the same square root convergence before the curve flattens off. The exact value of ℓ_{\max} where this transition happens increases as the impact parameter approaches R .

For the penetrating trajectories shown in Fig. 5 we find signs of the same slow convergence around the SPP accumulation point. This is masked in our convergence plots by the fact that the BP peak diverges. The source of the divergence lies in the decomposition of the EEL probability into two competing contributions stemming from the bulk and the Begrenzung terms. As illustrated in Figs. 5a and c, the two terms produce divergences of opposite sign; the negative Begrenzung term diverges linearly for increasing multipole order ℓ_{\max} , whereas the positive bulk term diverges logarithmically for increasing momentum cutoff q_c [see Eqs. (7a) and (7c)]. As our computational resources do not allow driving ℓ and q_c to infinity, once one of the two parameters is truncated to a certain cutoff value, the other has to be adjusted accordingly. Figs. 5b and d show that the different values

of ℓ and q_c , respectively, affect the spectra in the energy window between the SPP and BP modes.

B. EELS of NPs with surface roughness

The synthesis of spherical metallic NPs, as the ones studied in the present work, is routinely done with colloidal chemistry, for a large variety of materials and NP shapes [57, 58]. However, despite being able to accurately control the NP size, assuring a smooth surface is rather challenging. Typically the structures exhibit protuberances on the surface, which can be responsible for symmetry breaking [59, 60], hot spots in dimers [61, 62] and picocavities [63, 64], or energy shifts of the LSPs [65]. Within the DGTD method, surface texture can be easily implemented on top of the perfect spherical mesh and incorporated in the numerical calculations. Here, we follow the prescription presented in Ref. [66] to implement the desired roughness as a radius variation derived from Gaussian white noise, with a correlation length of 10 nm and two different values for the root-mean square (rms) amplitude (see details in section S.II.F of the SI).

In Fig. 6 we explore the effect of surface roughness on a spherical NP, described by the same Drude permittivity as in the previous section, now excited by an electron beam traveling with velocity $v = 0.7c$ (kinetic energy $\approx 200 \text{ keV}$) at distance $b = 100 \text{ nm}$ from its center. We probe meshes of two degrees of surface roughness on top of the NP of nominal radius $R = 75 \text{ nm}$, namely $\text{rms} = 2 \text{ nm}$ and 4 nm . Since the breaking of the spherical symmetry introduces a dependence on the electron propagation direction, and on the mesh morphology, in Fig. 6 we plot the *average* EEL probability, corresponding to the average values obtained for 6 different meshes. The resulting spectra for $\text{rms} = 2 \text{ nm}$ and 4 nm (dark red and blue curves, respectively) deviate notably from that of a smooth sphere (gray shaded area). Firstly, we observe an increasing redshift of the spectra with increasing degree of roughness, in agreement with experimental observations of corrugated plasmonic NPs [65]. The energy shift is most evident for the broad dipolar mode at around $\sim 2 \text{ eV}$, and is foremost the result of the area increase of the rough surface as compared to the smooth NP. Evaluation of this area from the mesh parameters yields an effective radius of $R_{\text{eff}} = 76.2 \text{ nm}$ for $\text{rms} = 2 \text{ nm}$, and $R_{\text{eff}} = 79.6 \text{ nm}$ for $\text{rms} = 4 \text{ nm}$. Indeed the EEL spectra of smooth spheres of said effective radii reproduce accurately the position of the dipolar mode (see Fig. S.9 in the SI).

In addition to the redshift, the spectra of the corrugated NPs feature a large number of low-intensity peaks. These new spectral features are the result of two factors. Due to the breaking of the spherical symmetry, the prior degenerate modes associated with the same angular momentum ℓ but different m number, now exhibit a small energy difference. As a result of the lift of the degeneracy, the sharp peaks observed in the spectrum of the

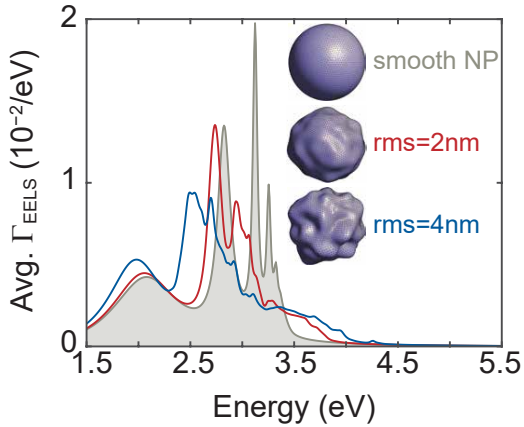


FIG. 6. Average EEL probability in the interaction between a spherical NP featuring surface roughness and an electron beam passing with velocity $v = 0.7c$ (kinetic energy ≈ 200 keV) at distance $b = 100$ nm. The solid lines correspond to NPs, whose shapes deviate from that of a perfectly smooth sphere of radius $R = 75$ nm (gray shaded area) by root-mean square roughness values $\text{rms} = 2$ nm (dark red curve) and $\text{rms} = 4$ nm (dark blue curve). The average EEL probability corresponds to the average values obtained with DGTD for 6 different rough meshes characterized by the same rms.

smooth NP are suppressed and, depending on the size of this energy difference with respect to the linewidth of the degenerate mode, they are either split or broadened. Moreover, additional spectral features may arise from hot-spots, namely protuberances of large curvature that strongly enhance and confine the incident field [64]. It is important to note here that, as the features become increasingly smaller, a rigorous description of the system requires the implementation of nonlocal effects in the method [67, 68], which effectively introduces a cutoff in the scattering from large wavevector components [69, 70].

IV. CONCLUSION

We have presented an analytic and a numerical method for the study of spherical structures excited by fast electron beams. Based on Mie theory, we have derived formulas for the calculation of the EEL and CL probability that are valid for both aloof and penetrating electron beams, as is typically the practice in EEL and CL measurements. Focusing on the plasmon oscillations of a metallic NP as a testbed, we compared the analytic theory with numerical simulations performed using the DGTD method,

and found excellent agreement. We discussed the applicability and limitations of each method, particularly for grazing trajectories and at energies near the surface- and bulk-plasmon resonances, and showcased the flexibility of the DGTD method by studying a NP with different degrees of surface corrugation, which can lead to resonance shifts and splittings due to the lifting of mode degeneracy. We thus believe that both methods are essential and complementary for exploring collective optical excitations in matter and for interpreting experimental observations.

ACKNOWLEDGMENTS

We thank F. Intravaia, C. Maciel-Escudero, and B. Beverungen for stimulating discussions. K. B. acknowledges funding by the German Research Foundation (DFG) in the framework of the Collaborative Research Center 1375 “Nonlinear Optics down to Atomic Scales (NOA)” (Project No. 398816777). N. A. M. is a VILLUM Investigator supported by VILLUM Fonden (grant No. 16498). The Center for Polariton-driven Light-Matter Interactions (POLIMA) is funded by the Danish National Research Foundation (Project No. DNRF165).

AUTHOR CONTRIBUTION

P. E. S and W. Z. contributed equally to this work. P. E. S performed the analytic study and W. Z. the DGTD simulations. All authors participated in the discussion of the results and the writing of the manuscript.

APPENDIX

The field expansion coefficients entering Eqs. (4) and (7) are given by

$$b_{\ell m}^{\text{I}} = T_{M_\ell}^{11} b_{\ell m}^{0,\text{I}} + T_{M_\ell}^{21} b_{\ell m}^{0,\text{II}} - b_{\ell m}^{0,\text{II}}, \quad (11a)$$

$$b_{\ell m}^{\text{II}} = T_{M_\ell}^{12} b_{\ell m}^{0,\text{I}} + T_{M_\ell}^{22} b_{\ell m}^{0,\text{II}} - b_{\ell m}^{0,\text{I}}|_{\text{air}}, \quad (11b)$$

$$a_{\ell m}^{\text{I}} = T_{E_\ell}^{11} a_{\ell m}^{0,\text{I}} + T_{E_\ell}^{21} a_{\ell m}^{0,\text{II}} - a_{\ell m}^{0,\text{II}}, \quad (11c)$$

$$a_{\ell m}^{\text{II}} = T_{E_\ell}^{12} a_{\ell m}^{0,\text{I}} + T_{E_\ell}^{22} a_{\ell m}^{0,\text{II}} - a_{\ell m}^{0,\text{I}}|_{\text{air}}, \quad (11d)$$

where $a/b_{\ell m}^{0,\text{I}}$ and $a/b_{\ell m}^{0,\text{II}}$ correspond to the fields generated by the part of the electron trajectory lying in region I (inside the NP) and region II (outside the NP), respectively, as illustrated in Fig. 1. The coefficients are found by the following expressions

$$b_{\ell m}^{0,\text{II}} = -\frac{ik_0^2 e}{\varepsilon_0 \omega} \frac{m}{\sqrt{\ell(\ell+1)}} \left[\mathcal{M}_{\ell m} K_m \left(\frac{\omega b}{v\gamma_0} \right) - ik_0 \int_{-z_e}^{z_e} dz \exp(i\omega z/v) h_\ell^+(k_0 r) Y_\ell^m(\theta, 0) \right], \quad (12a)$$

$$a_{\ell m}^{0,\text{II}} = \frac{ik_0^2 e}{\varepsilon_0 \omega} \frac{1}{\sqrt{\ell(\ell+1)}} \left[\frac{\mathcal{N}_{\ell m}}{\beta \gamma_0} K_m \left(\frac{\omega b}{v \gamma_0} \right) - \frac{i}{b} \int_{-z_e}^{z_e} dz \exp(i\omega z/v) \left\{ \mathcal{H}_{\ell m}^+(k_0 z) + \mathcal{H}_{\ell m}^-(k_0 z) \right\} \right], \quad (12b)$$

$$b_{\ell m}^{0,\text{I}} = -\frac{ik_0^2 e}{\varepsilon_0 \omega} \frac{m}{\sqrt{\ell(\ell+1)}} ik \int_{-z_e}^{z_e} dz \exp(i\omega z/v) j_\ell(kr) Y_\ell^m(\theta, 0), \quad (12c)$$

and

$$a_{\ell m}^{0,\text{I}} = \frac{ik_0^2 e}{\varepsilon_0 \omega} \frac{1}{\sqrt{\ell(\ell+1)}} \frac{i}{b} \int_{-z_e}^{z_e} dz \exp(i\omega z/v) \left\{ \mathcal{J}_{\ell m}^-(kz) + \mathcal{J}_{\ell m}^+(kz) \right\}. \quad (12d)$$

In Eqs. (11) the notation $a/b_{\ell m}^{0,\text{I}}|_{\text{air}}$ indicates evaluation of the terms in Eqs. (12c) and (12d) in air ($\varepsilon = 1$, $k = k_0$). Moreover, in Eqs. (7) and (12) we have set

$$\mathcal{M}_{\ell m} = i^{\ell+m} \sqrt{\frac{2\ell+1}{\pi} \frac{(\ell-m)!}{(\ell+m)!}} \frac{(2m-1)!!}{(\beta \gamma_0)^m} G_{\ell-m}^{m+1/2} \left(\frac{1}{\beta} \right), \quad (13)$$

and

$$\mathcal{N}_{\ell m} = c_\ell^m \mathcal{M}_{\ell m+1} - c_\ell^{-m} \mathcal{M}_{\ell m-1}, \quad (14)$$

with

$$c_\ell^m = \frac{1}{2} \sqrt{(\ell-m)(\ell+m+1)}, \quad (15)$$

where $G_{\ell-m}^{m+1/2}(x)$ is the Gegenbauer polynomial. Eq. (13) holds for $m \geq 0$, while $\mathcal{M}_{\ell-m} = (-1)^m \mathcal{M}_{\ell m}$. Additionally, in Eqs. (7) and (12), we have set

$$\begin{aligned} \mathcal{F}_{\ell m}^\pm(k_n z) = & \mp c_\ell^{\pm m} \left\{ \frac{k_n b^2}{r} f'_\ell(k_n r) Y_\ell^{m \pm 1}(\theta, 0) \right. \\ & \pm \frac{z b}{r^2} f_\ell(k_n r) [c_\ell^{\pm m+1} Y_\ell^{m \pm 2}(\theta, 0) - c_\ell^{\pm m} Y_\ell^m(\theta, 0)] \\ & \left. + (1 \pm m) f_\ell(k_n r) Y_\ell^{m \pm 1}(\theta, 0) \right\}. \end{aligned} \quad (16)$$

Eq. (16) holds for any type of spherical Bessel function $f_\ell(k_n r)$ evaluated in any medium n (the prime here and on any other Bessel function denotes the derivative of the

function with respect to the argument). In particular, in Eq. (12d) we use expression (16) for $\mathcal{F}_{\ell m}^\pm(k_n z) = \mathcal{J}_{\ell m}^\pm(kz)$ and $f_\ell = j_\ell$, whereas in Eq. (12b) we use $\mathcal{F}_{\ell m}^\pm(k_n z) = \mathcal{H}_{\ell m}^\pm(k_0 z)$ and $f_\ell = h_\ell^+$.

Finally in Eqs. (11) we have introduced the Mie coefficients

$$T_{E_\ell}^{22} = \frac{\varepsilon j_\ell(kR) \Psi'_\ell(k_0 R) - \Psi'_\ell(kR) j_\ell(k_0 R)}{h_\ell^+(k_0 R) \Psi'_\ell(kR) - \varepsilon \xi'_\ell(k_0 R) j_\ell(kR)}, \quad (17a)$$

$$T_{M_\ell}^{22} = \frac{j_\ell(kR) \Psi'_\ell(k_0 R) - \Psi'_\ell(kR) j_\ell(k_0 R)}{h_\ell^+(k_0 R) \Psi'_\ell(kR) - \xi'_\ell(k_0 R) j_\ell(kR)}, \quad (17b)$$

$$T_{E_\ell}^{21} = -\frac{i\sqrt{\varepsilon}/(k_0 R)}{h_\ell^+(k_0 R) \Psi'_\ell(kR) - \varepsilon \xi'_\ell(k_0 R) j_\ell(kR)}, \quad (17c)$$

$$T_{M_\ell}^{21} = -\frac{i/(k_0 R)}{h_\ell^+(k_0 R) \Psi'_\ell(kR) - \xi'_\ell(k_0 R) j_\ell(kR)}, \quad (17d)$$

$$T_{E_\ell}^{11} = \frac{\varepsilon \xi'_\ell(k_0 R) h_\ell^+(kR) - h_\ell^+(k_0 R) \xi'_\ell(kR)}{h_\ell^+(k_0 R) \Psi'_\ell(kR) - \varepsilon \xi'_\ell(k_0 R) j_\ell(kR)}, \quad (17e)$$

$$T_{M_\ell}^{11} = \frac{\xi'_\ell(k_0 R) h_\ell^+(kR) - h_\ell^+(k_0 R) \xi'_\ell(kR)}{h_\ell^+(k_0 R) \Psi'_\ell(kR) - \xi'_\ell(k_0 R) j_\ell(kR)}, \quad (17f)$$

$$T_{E_\ell}^{12} = -\frac{i/(k_0 R)}{h_\ell^+(k_0 R) \Psi'_\ell(kR) - \varepsilon \xi'_\ell(k_0 R) j_\ell(kR)}, \quad (17g)$$

$$T_{M_\ell}^{12} = -\frac{i/(\sqrt{\varepsilon} k_0 R)}{h_\ell^+(k_0 R) \Psi'_\ell(kR) - \xi'_\ell(k_0 R) j_\ell(kR)}, \quad (17h)$$

where we have adopted the notation of the Riccati–Bessel functions $\Psi_\ell(x) = x j_\ell(x)$ and $\xi_\ell(x) = x h_\ell^+(x)$.

* elli@mci.sdu.dk

† kurt.busch@physik.hu-berlin.de

‡ cwo@mci.sdu.dk

- [1] F. J. García de Abajo, *Rev. Mod. Phys.* **82**, 209 (2010).
- [2] H. Watanabe, *J. Phys. Soc. Japan* **11**, 112 (1956).
- [3] R. H. Ritchie, *Phys. Rev.* **106**, 874 (1957).
- [4] N. Yamamoto, K. Araya, and F. J. García de Abajo, *Phys. Rev. B* **64**, 205419 (2001).
- [5] E. J. R. Vesseur, R. de Waele, M. Kuttge, and A. Polman, *Nano Lett.* **7**, 2843 (2007).

- [6] T. Coenen, J. van de Groep, and A. Polman, *ACS Nano* **7**, 1689 (2013).
- [7] T. Matsukata, N. Matthaikakakis, T.-a. Yano, M. Hada, T. Tanaka, N. Yamamoto, and T. Sannomiya, *ACS Photonics* **6**, 2320 (2019).
- [8] S. Fiedler, P. E. Stamatopoulou, A. Assadillayev, C. Wolff, H. Sugimoto, M. Fujii, N. A. Mortensen, S. Raza, and C. Tserkezis, *Nano Lett.* **22**, 2320 (2022).
- [9] M. J. Lagos, A. Trügler, U. Hohenester, and P. E. Batson, *Nature* **543**, 529 (2017).

- [10] F. S. Hage, D. M. Kepaptsoglou, Q. M. Ramasse, and L. J. Allen, *Phys. Rev. Lett.* **122**, 016103 (2019).
- [11] C. Maciel-Escudero, A. Konečná, R. Hillenbrand, and J. Aizpurua, *Phys. Rev. B* **102**, 115431 (2020).
- [12] A. Polman, M. Kociak, and F. J. García de Abajo, *Nat. Mater.* **18**, 1158 (2019).
- [13] F. J. García de Abajo and V. Di Giulio, *ACS Photonics* **8**, 945 (2021).
- [14] R. F. Egerton, *Electron energy-loss spectroscopy in the electron microscope* (Springer Science & Business Media, New York, 2011).
- [15] Y. Wu, G. Li, and J. P. Camden, *Chem. Rev.* **118**, 2994 (2018).
- [16] P. Batson and J. Silcox, *Phys. Rev. B* **27**, 5224 (1983).
- [17] F.-P. Schmidt, H. Ditlbacher, U. Hohenester, A. Hohenau, F. Hofer, and J. R. Krenn, *Nano Lett.* **12**, 5780 (2012).
- [18] A. L. Koh, K. Bao, I. Khan, W. E. Smith, G. Kothleitner, P. Nordlander, S. A. Maier, and D. W. McComb, *ACS Nano* **3**, 3015 (2009).
- [19] B. Barwick, H. S. Park, O.-H. Kwon, J. S. Baskin, and A. H. Zewail, *Science* **322**, 1227 (2008).
- [20] B. Barwick, D. J. Flannigan, and A. H. Zewail, *Nature* **462**, 902 (2009).
- [21] T. L. Ferrell and P. M. Echenique, *Phys. Rev. Lett.* **55**, 1526 (1985).
- [22] R. Garcia-Molina, A. Gras-Marti, and R. H. Ritchie, *Phys. Rev. B* **31**, 121 (1985).
- [23] A. Rivacoba, N. Zabala, and P. M. Echenique, *Phys. Rev. Lett.* **69**, 3362 (1992).
- [24] N. Zabala, A. Rivacoba, and P. M. Echenique, *Surf. Sci.* **209**, 465 (1989).
- [25] P. M. Echenique, J. Bausells, and A. Rivacoba, *Phys. Rev. B* **35**, 1521 (1987).
- [26] R. H. Ritchie and A. Howie, *Phil. Mag. A* **58**, 753 (1988).
- [27] E. Kröger, *Z. Phys.* **235**, 403 (1970).
- [28] F. J. García de Abajo, *Phys. Rev. B* **59**, 3095 (1999).
- [29] F. S. Hage, G. Radtke, D. M. Kepaptsoglou, M. Lazzeri, and Q. M. Ramasse, *Science* **367**, 1124 (2020).
- [30] A. B. Yankovich, B. Munkhbat, D. G. Baranov, J. Cuadra, E. Olsen, H. Lourenço-Martins, L. H. G. Tizei, M. Kociak, E. Olsson, and T. Shegai, *Nano Lett.* **19**, 8171 (2019).
- [31] R. Pogorzelski and C. Yeh, *Phys. Rev. A* **8**, 137 (1973).
- [32] V. L. Ginzburg, *Phys. Usp.* **39**, 973 (1996).
- [33] N. Yamamoto, H. Sugiyama, and A. Toda, *Proc. R. Soc. London. Ser. A* **452**, 2279 (1996).
- [34] B. Gallinet, J. Butet, and O. J. F. Martin, *Laser Photonics Rev.* **9**, 577 (2015).
- [35] F. J. García de Abajo and A. Howie, *Phys. Rev. B* **65**, 115418 (2002).
- [36] U. Hohenester, *Comput. Phys. Commun.* **185**, 1177 (2014).
- [37] J. Pomplun, S. Burger, L. Zschiedrich, and F. Schmidt, *Phys. Status Solidi B* **244**, 3419 (2007).
- [38] S. Burger, J. Pomplun, and F. Schmidt, “Finite element methods for computational nano-optics,” in *Encyclopedia of Nanotechnology*, edited by B. Bhushan (Springer Netherlands, Dordrecht, 2012) pp. 837–843.
- [39] P. Das, T. K. Chini, and J. Pond, *J. Phys. Chem. C* **116**, 15610 (2012).
- [40] Y. Cao, A. Manjavacas, N. Large, and P. Nordlander, *ACS Photonics* **2**, 369 (2015).
- [41] J. S. Hesthaven and T. Warburton, *Nodal discontinuous Galerkin methods: algorithms, analysis, and applications* (Springer Science & Business Media, New York, 2007).
- [42] C. Matyssek, J. Niegemann, W. Hergert, and K. Busch, *Photon. Nanostruct. Fundam. Appl.* **9**, 367 (2011).
- [43] K. Busch, M. König, and J. Niegemann, *Laser Photonics Rev.* **5**, 773 (2011).
- [44] M. Husnik, F. von Cube, S. Irsen, S. Linden, J. Niegemann, K. Busch, and M. Wegener, *Nanophotonics* **2**, 241 (2013).
- [45] M. Prämassing, T. Kiel, S. Irsen, K. Busch, and S. Linden, *Phys. Rev. B* **103**, 115403 (2021).
- [46] A. A. Maradudin and D. L. Mills, *Phys. Rev. B* **11**, 1392 (1975).
- [47] A. A. Maradudin and E. R. Méndez, *Sci. Prog.* **90**, 161 (2007).
- [48] G. Mie, *Ann. Phys.* **330**, 377 (1908).
- [49] J. D. Jackson, *Classical Electrodynamics*, 3rd ed. (John Wiley & Sons, New York, 1998).
- [50] A. A. Lucas and M. Šunjić, *Prog. Surf. Sci.* **2**, 75 (1972).
- [51] C. F. Bohren and D. R. Huffman, *Absorption and Scattering of Light by Small Particles* (John Wiley & Sons, New York, 1983).
- [52] P. E. Batson, A. Reyes-Coronado, R. G. Barrera, A. Rivacoba, P. M. Echenique, and J. Aizpurua, *Nano Lett.* **11**, 3388 (2011).
- [53] T. Christensen, W. Yan, S. Raza, A.-P. Jauho, N. A. Mortensen, and M. Wubs, *ACS Nano* **8**, 1745 (2014).
- [54] G. P. Zouros, G. D. Kolezas, N. A. Mortensen, and C. Tserkezis, *Phys. Rev. B* **101**, 085416 (2020).
- [55] P. A. D. Gonçalves and F. J. García de Abajo, *Nano Lett.* **23**, 4242 (2023).
- [56] M. Moeferd, *Nonlocal and nonlinear properties of plasmonic nanostructures within the hydrodynamic Drude model*, Ph.D. thesis, Humboldt Universität zu Berlin (Germany) (2017).
- [57] S. Link and M. A. El-Sayed, *J. Phys. Chem. B* **103**, 4212 (1999).
- [58] M. Grzelczak, J. Vermant, E. M. Furst, and L. M. Liz-Marzán, *ACS Nano* **4**, 3591 (2010).
- [59] J. Nappa, G. Revillod, I. Russier-Antoine, E. Benichou, C. Jonin, and P. Brevet, *Phys. Rev. B* **71**, 165407 (2005).
- [60] A. Salomon, M. Zielinski, R. Kolkowski, J. Zyss, and Y. Prior, *J. Phys. Chem. C* **117**, 22377 (2013).
- [61] P. Zheng, S. K. Cushing, S. Suri, and N. Wu, *Phys. Chem. Chem. Phys.* **17**, 21211 (2015).
- [62] J. H. Yoon, F. Selbach, L. Schumacher, J. Jose, and S. Schlücker, *ACS Photonics* **6**, 642 (2019).
- [63] F. Benz, M. K. Schmidt, A. Dreismann, R. Chikkaraddy, Y. Zhang, A. Demetriadou, C. Carnegie, H. Ohadi, B. de Nijs, R. Esteban, J. Aizpurua, and J. J. Baumberg, *Science* **354**, 726 (2016).
- [64] M. Urbietta, M. Barbry, Y. Zhang, P. Koval, D. Sánchez-Portal, N. Zabala, and J. Aizpurua, *ACS Nano* **12**, 585 (2018).
- [65] J. Rodríguez-Fernández, A. M. Funston, J. Pérez-Juste, R. A. Álvarez-Puebla, L. M. Liz-Marzán, and P. Mulvaney, *Phys. Chem. Chem. Phys.* **11**, 5909 (2009).
- [66] F. Loth, T. Kiel, K. Busch, and P. T. Kristensen, *J. Opt. Soc. Am. B* **40**, B1 (2023).
- [67] P. E. Stamatopoulou and C. Tserkezis, *Opt. Mater. Express* **12**, 1869 (2022).
- [68] G. Wegner, D.-N. Huynh, N. A. Mortensen, F. Intravaia, and K. Busch, *Phys. Rev. B* **107**, 115425 (2023).
- [69] A. Wiener, A. F. Fernández-Domínguez, A. P. Horsfield,

- J. B. Pendry, and S. A. Maier, [Nano Lett.](#) **12**, 3308 (2012).
- [70] N. A. Mortensen, [Nanophotonics](#) **10**, 2563 (2021).